SUPLLEMENTARY INFORMATION (SI)

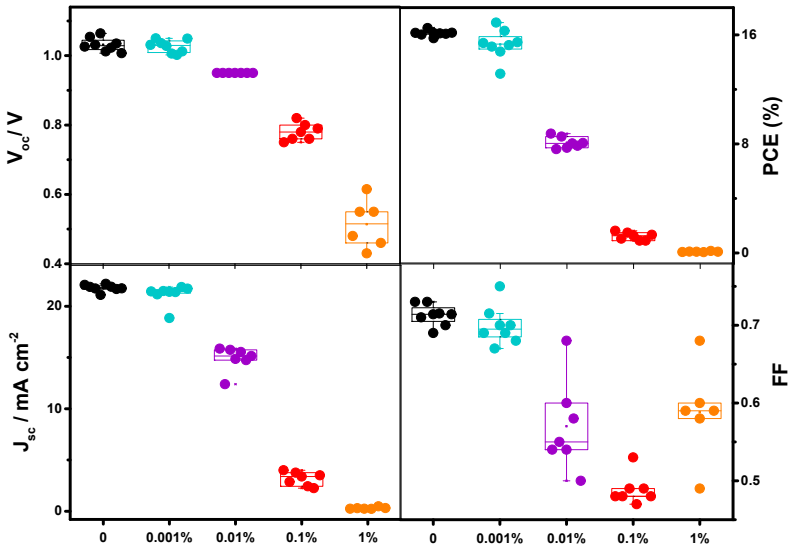

Figure S1. Characteristic parameters of solar cells containing $CH_3NH_3PbI_3$ show exactly the same trend with addition of Bi as the triple cation perovskite.

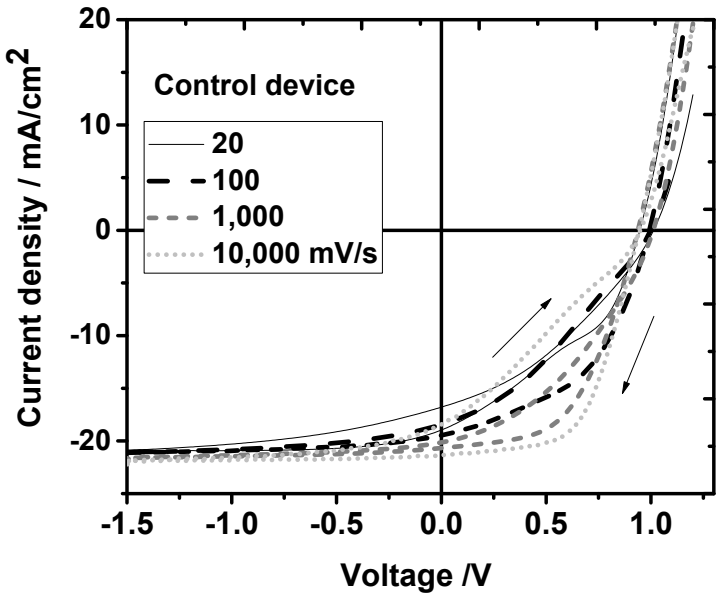

Figure S2. *JV* hysteresis loops starting from 1.2 V for various voltage sweep rates measured at a device with 0% Bi.

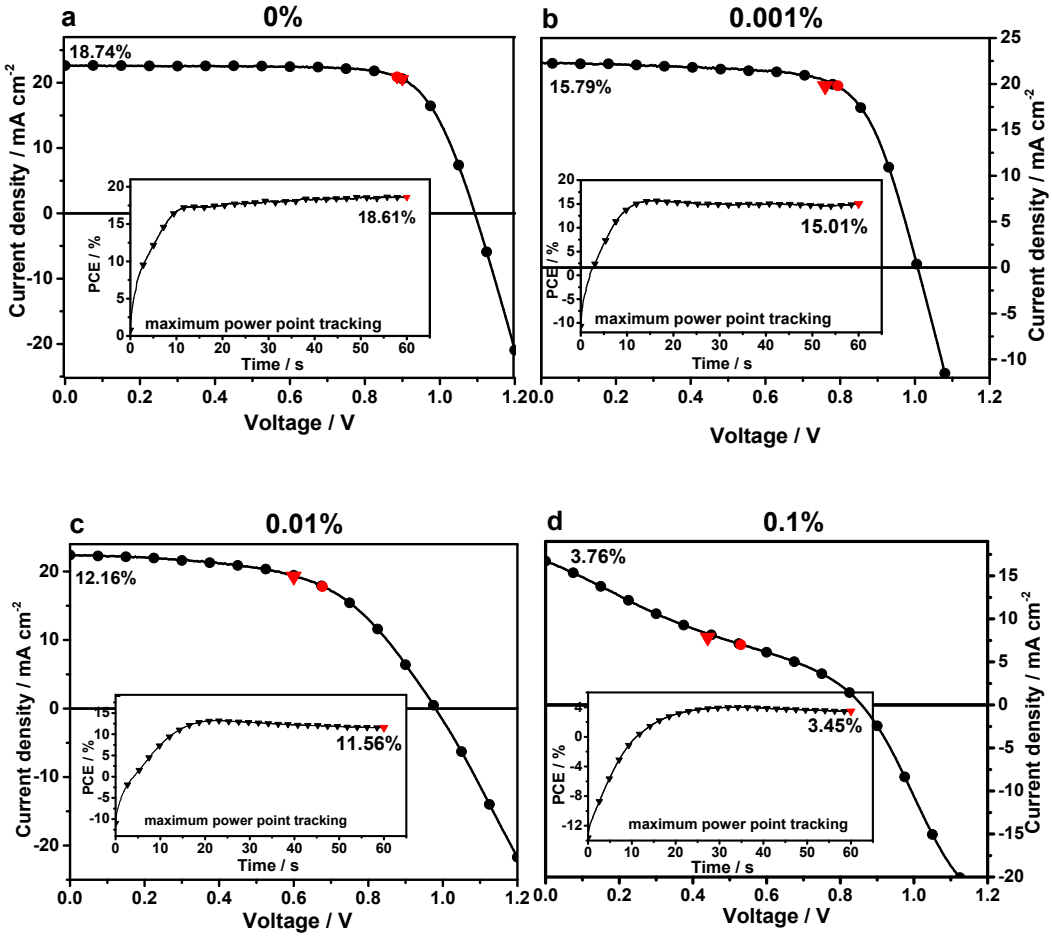
a
0%
18.74%
18.61%
maximum power point tracking
PCE / %
Time / s
Current density / mA cm-2
Voltage / V
b
0.001%
15.79%
15.01%
maximum power point tracking
PCE / %
Time / s
Current density / mA cm-2
Voltage / V
c
0.01%
12.16%
11.56%
maximum power point tracking
PCE / %
Time / s
Current density / mA cm-2
Voltage / V
d
0.1%
3.76%
3.45%
maximum power point tracking
PCE / %
Time / s
Current density / mA cm-2
Voltage / V

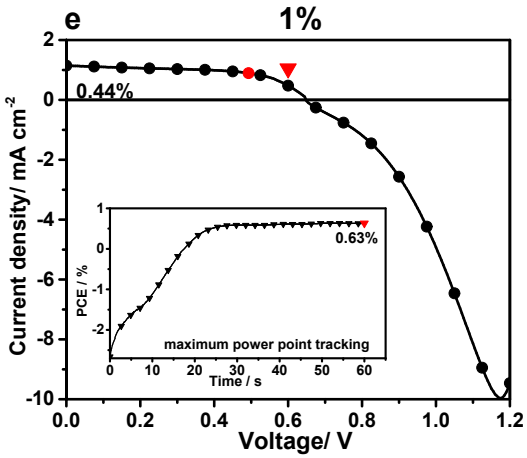

Figure S3. *JV* curves measured under the solar simulator (-100 mV/s) with marked maximum power point (MPP) (red circle) compared to the MPP obtained by 1 minutes of MPP tracking (inset, red triangle).

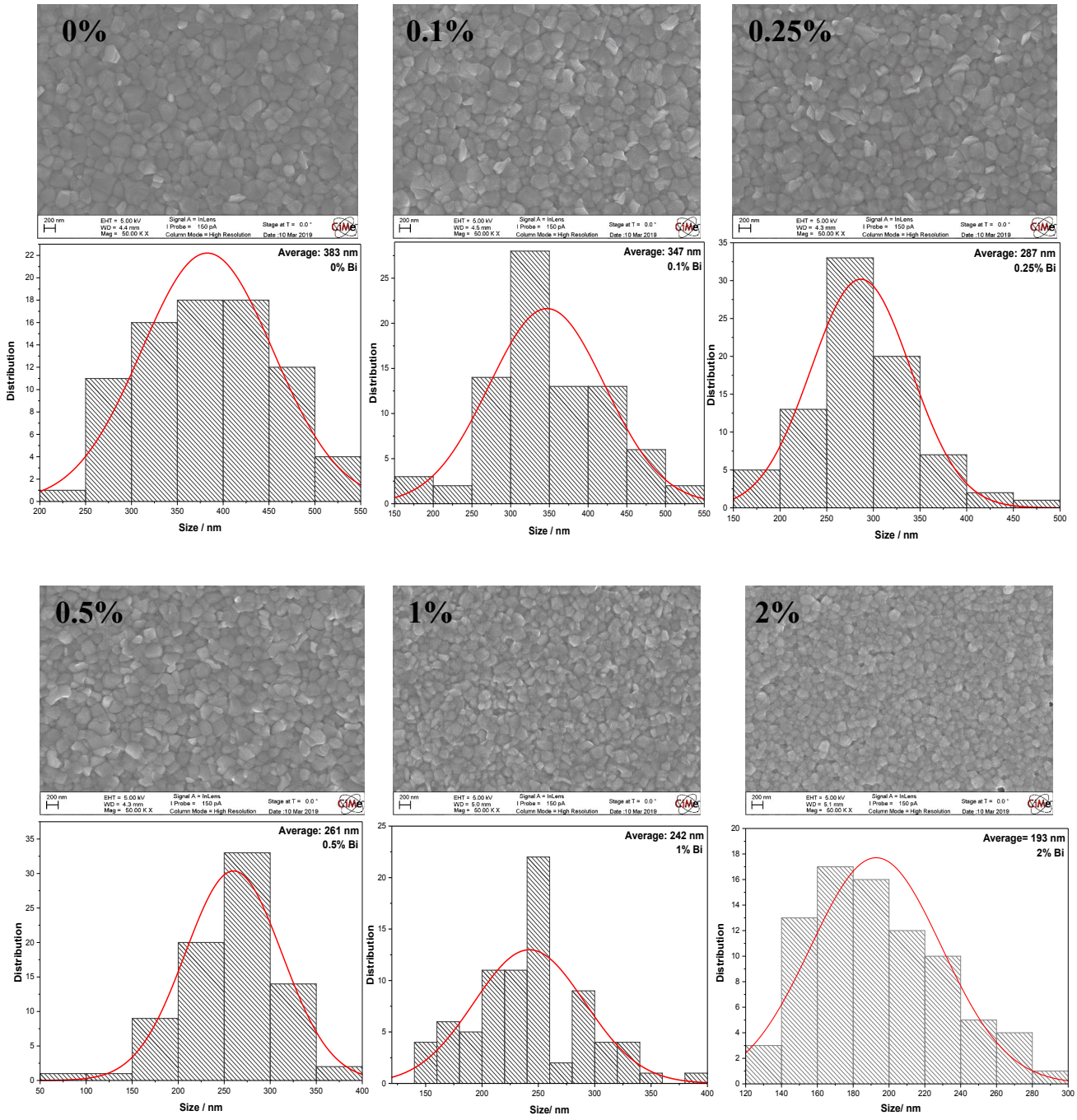

Figure S4. SEM images and histograms of the grain diameter distribution of samples with different Bi concentration.

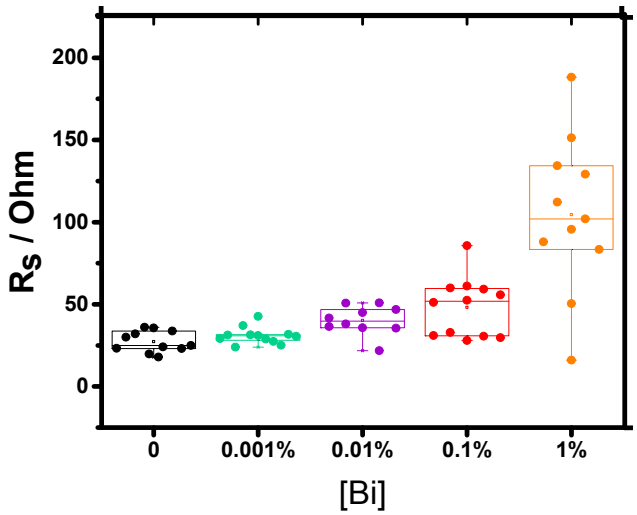

Figure S5. Phenomenological series resistance extracted from the differential slope of the current-voltage curve under forward bias. The values are estimates of an upper limit of the series resistance including lateral transport through the electrode, vertical transport, and the diode differential resistance.

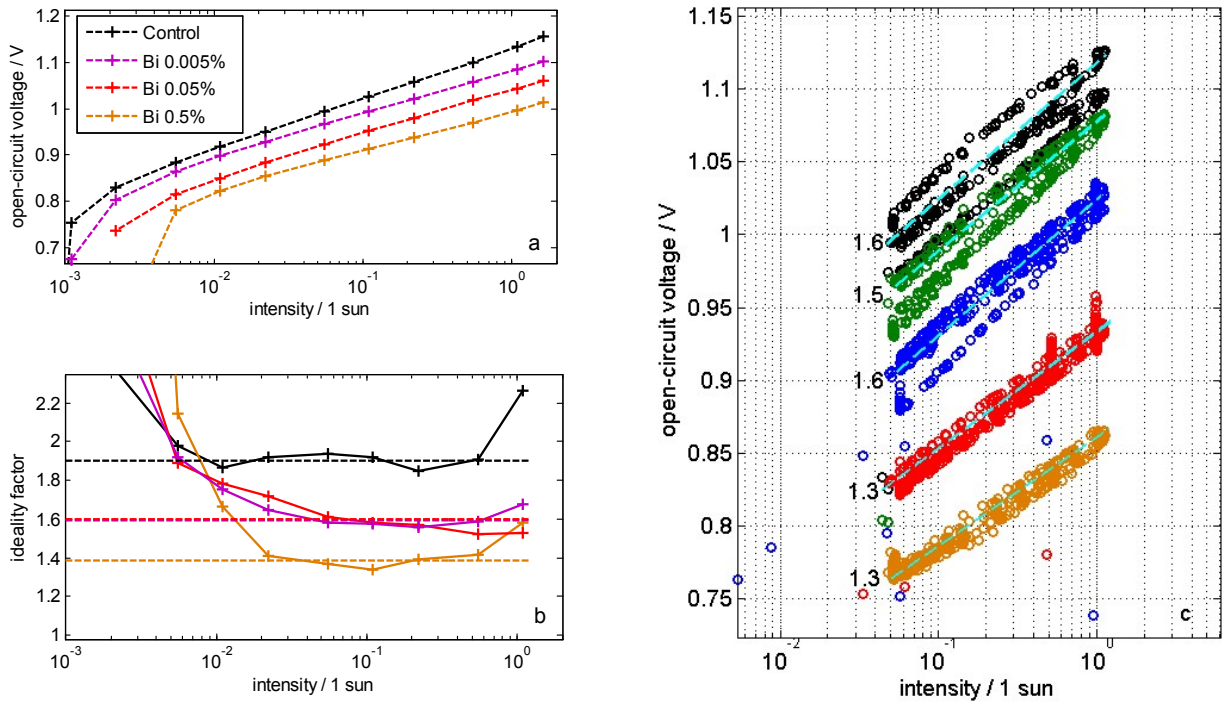

Figure S6. Recombination in full devices (a) V_{oc} as a function of illumination intensity. (b) Deduced ideality factors (averaged over three measurements, where the estimated error is in the range of 0.1). The dashed lines are the average value between 10^{-2} and 1 suns. An ideality factor of 1.6 is attributed to recombination in the bulk introduced by Bi. Comparing (a) and (b), we observe that the ideality factor decreases for devices with lower V_{oc}. (c) Another series of samples (0, 0.001, 0.01, 0.1, 1% Bi), where V_{oc} was measured by subsequent step wise intensity sweeps and all the data plotted vs light intensity. Different traces clearly indicate severe light soaking effects, which make it hard to extract an unambiguous value for the ideality factor. The dashed lines and numbers are just given as guide to the eye and in particular for the devices with higher V_{oc}, other lines could be plotted which lead to ideality factors spanning a range of 1.3 to 2. In general, adding Bi does not dramatically change the ideality factor within our accuracy, however reduces it slightly, which might indicate more recombination at regions with higher background charge carrier densities, either introduced by the Bi itself or closer to interfaces.

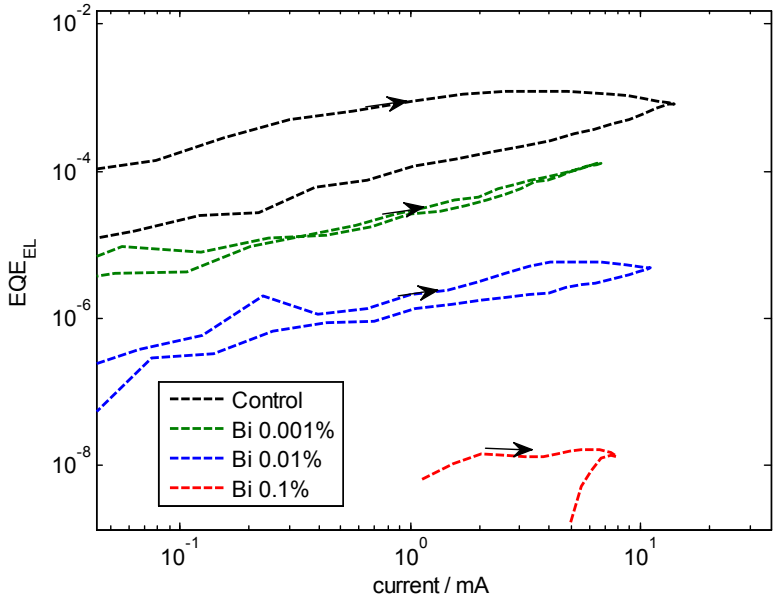

Figure S7. EQE EL versus injection current obtained by a *JV* sweep with a rate of 20 mV/s. In case of large hysteresis, the value from the forward sweep is used for Table 1 due to the instability introduced by high driving voltages, which temporarily reduces the EQE EL.

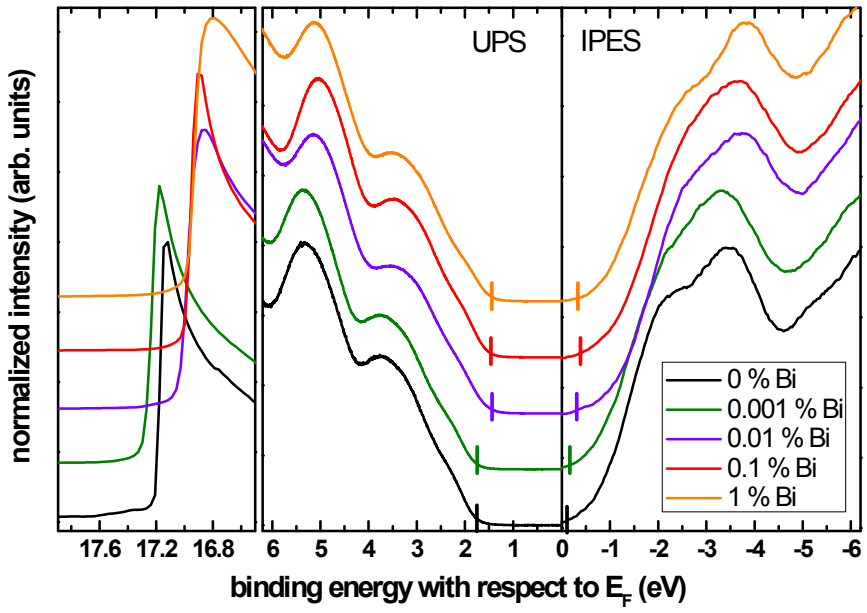

Figure S8. Combined UPS and IPES spectra of $Cs_{0.1}FA_{0.9}Pb(Br_{0.1}I_{0.9})_3$ films with different Bi concentration shown in a linear scale. Onsets of the valence band and conduction band (extracted by linear extrapolation of DOS) are marked by vertical lines. Extracted values are listed in table 2 in the main article.

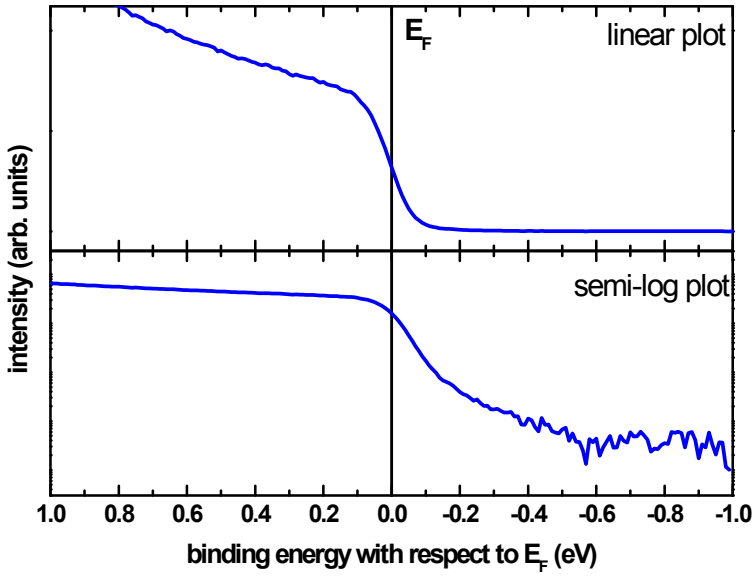

Figure S9. Example of a Fermi edge of a copper sample, measured by UPS. The upper graph is a linear representation of the intensity, showing that the binding energy scale is correctly calibrated, so E_F is positioned at the center of the Fermi edge. The lower panel shows the same measurement in a semi-log scale; here, the density above E_F is blown up, leading to an asymmetric look of E_F and the observation of occupied DOS seems to reach significantly above E_F, similar to the gap states observed in Fig. 7 of the main article.

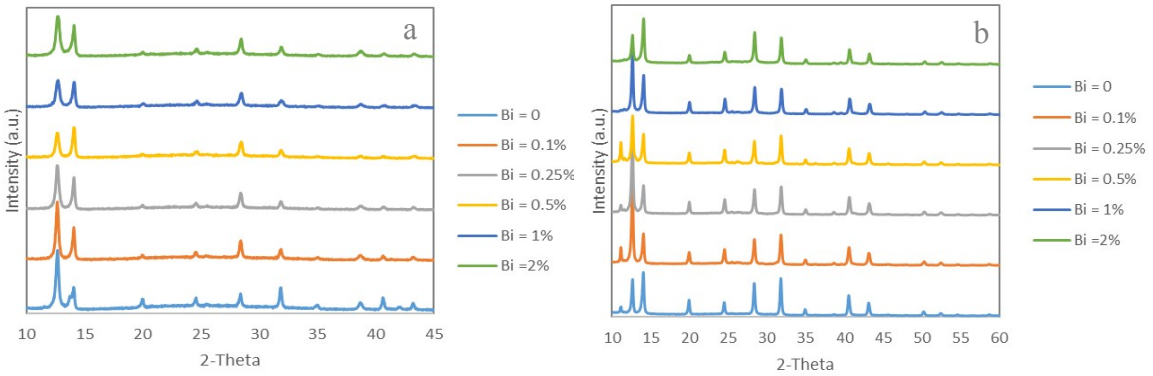

Figure S10. XRD pattern of Bi doped mixed cation perovskite thin-films. (a: Batch 1, fixed slits XRD; b: Batch 2, grazing incidence XRD). (An undefined impurity peak at 2θ = 11.2° is observed for some samples in Batch 2.)

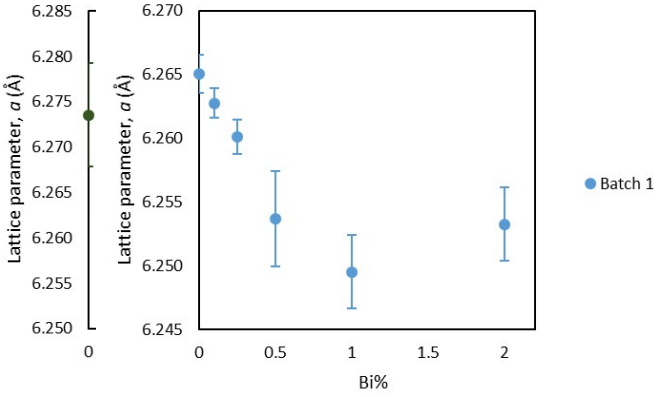

Figure S11. Effect of doping Bi on the lattice parameter in mixed-cation perovskite thin-films, whose spectra are shown in Figure S4.

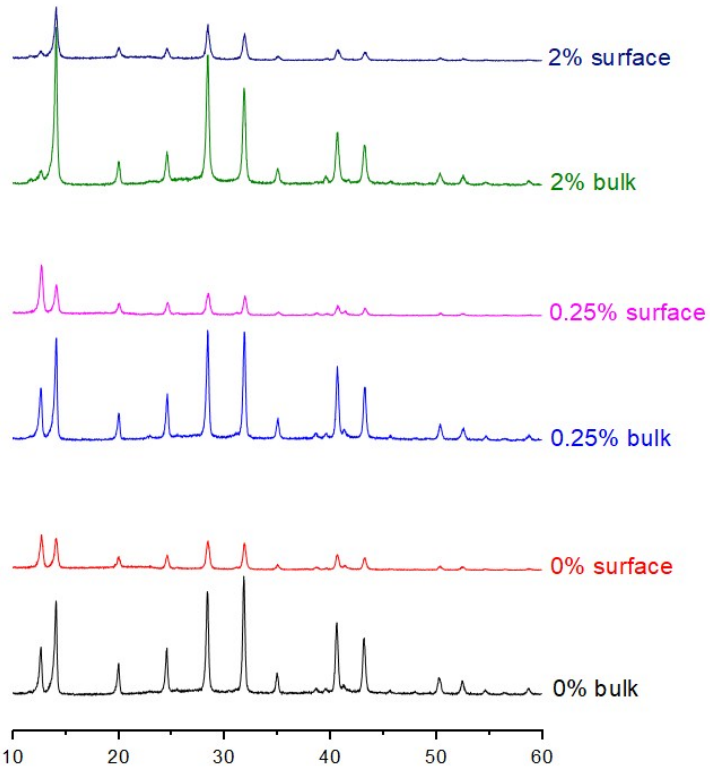

Figure S12. Grazing incidence X-ray diffraction conducted with incidence angle of 0.25° and 1° to measure the crystal structures at the film surface and bulk respectively (the critical penetration angle is 0.27° for methylammonium lead iodide). The same trend of lattice parameters was observed for the measurement at the surface and inside the bulk film (Table S2). A decrease in lattice parameters was confirmed as Bi is doped into the perovskite structure at both the surface and inside the bulk structure. The lattice parameters measured at the film surface is a little bit larger than the average lattice parameters inside the film.

Major impurity peaks observed 12.6° PbI_2 (001), 38.9° PbI_2 (003), 39.6° BiI_3 (009), 40.9° BiI_3 (300)

Details on the calculations

Bi_{Pb} defects: configuration, effect on the related orbitals.

Figure S13 illustrates the different structural characteristics of the two types of defect configurations discussed in the main text. The type one is highly symmetric, with similar values of the three I-Bi-I angles$^{\alpha}$, and all equilibrium values are $\geq 175°$. In the type two there is a pronounced asymmetry: the equilibrium value of one of the three I-Bi-I angles is ~ 170°. This has an effect on the structure of defect orbitals, as explained in detail below.

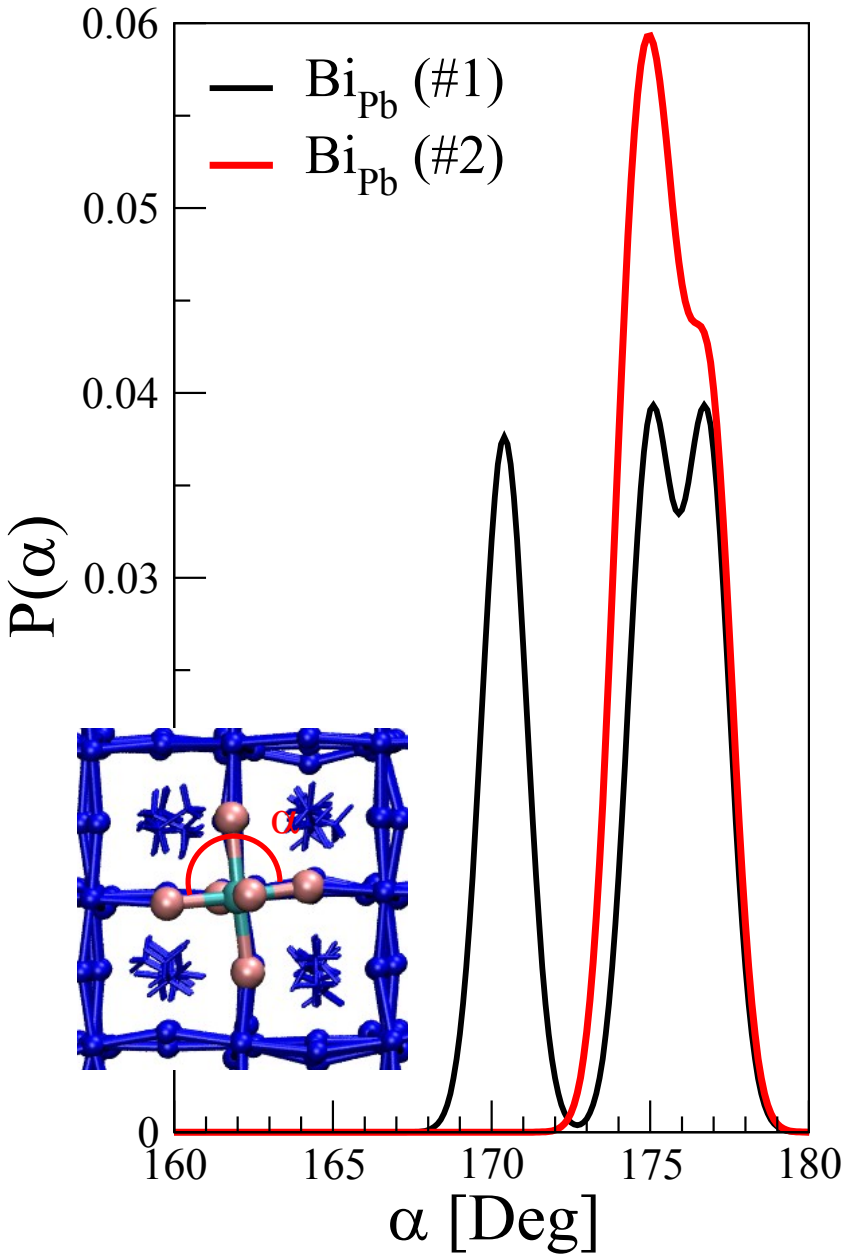

Figure S13. Distribution of the I-Bi-I angle α of triplets of atoms belonging to the same axis of BiI_6 octahedron (inset).

In the neutral defect, i.e. when the defect has captured an electron, the orbitals corresponding to the doping states are all made of an antibonding combination of Bi 6p, Pb 6p and I 5s atomic orbitals (Figs. 9b and **S14**), similar to the typical Pb 6p/I 5s CBM of undoped halide perovskites [1–3]. However, while the shallow doping states are relatively diffuse, involving all the Pb and I atoms belonging to the same row of Bi in the three lattice directions of the inorganic framework, the deep state is highly localized, and consists mainly of one Bi p orbital (p_z in the case shown in Figure 9b) with a minor contribution of nearest neighbor I 5s and Pb 6p orbitals. The different degree of localization and energy of the defect orbitals is due to the different local environment of Bi_{Pb}: the lower is the angle of the I-Bi-I triplet the lower (more stable) is the energy of the corresponding defect orbital. This is because a lower I-Bi-I angle reduces the negative overlapping among the atomic orbitals and thus the energy of the doping state[4]. This is seen by comparing the DOS of defects of type 1 and 2 (Figure 9).

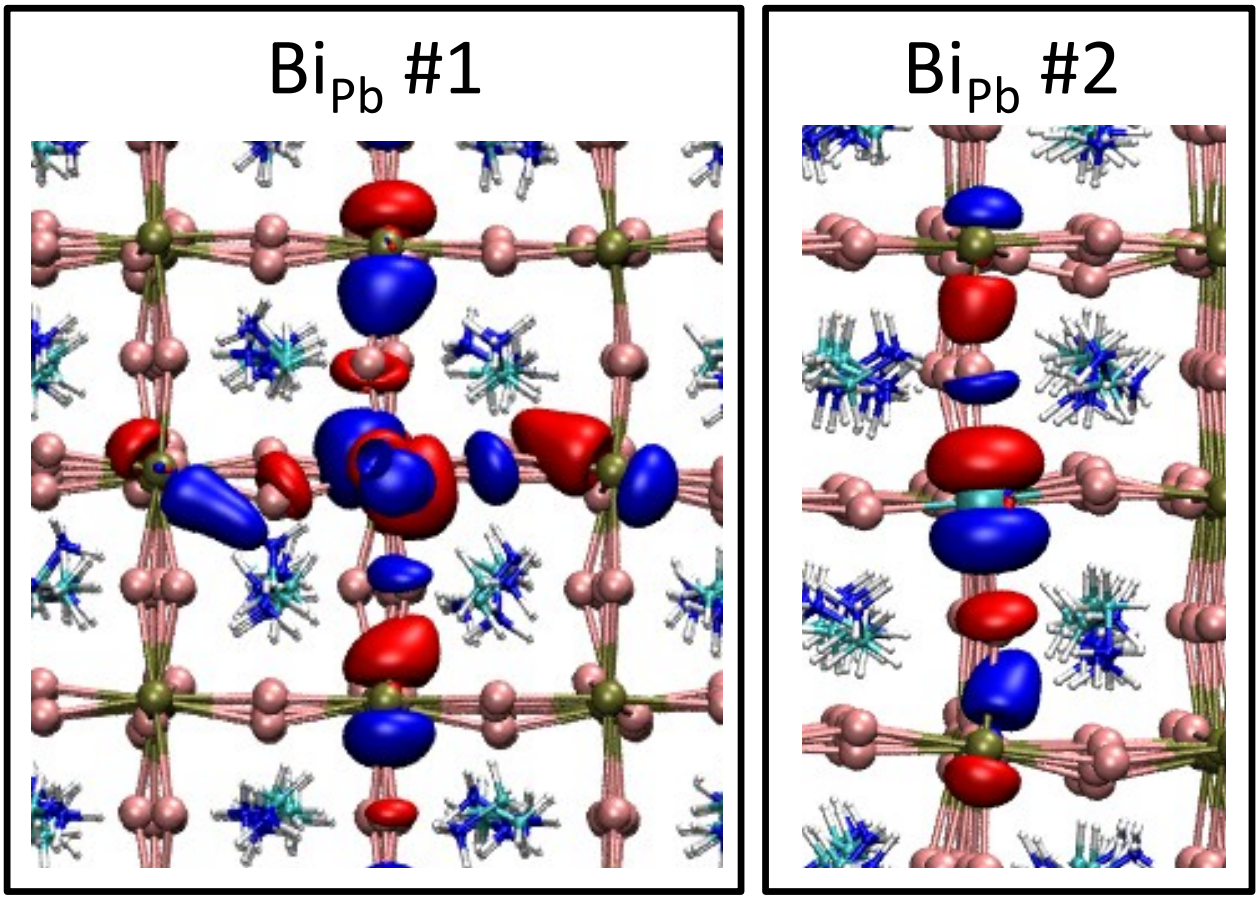

Figure S14. Isodensity plot of the occupied defect orbitals in neutral Bi_{Pb} defects of type 1 (left) and 2 (right). This figure is a zoom of one of the panels of Fig. 7.

Our calculations show that the five different defect configurations generated by the multi-step procedure described in the *Methods* section are consistent with either type 1 or 2, shallow and deep defect, respectively (Figure S15), in a ratio 1:4.

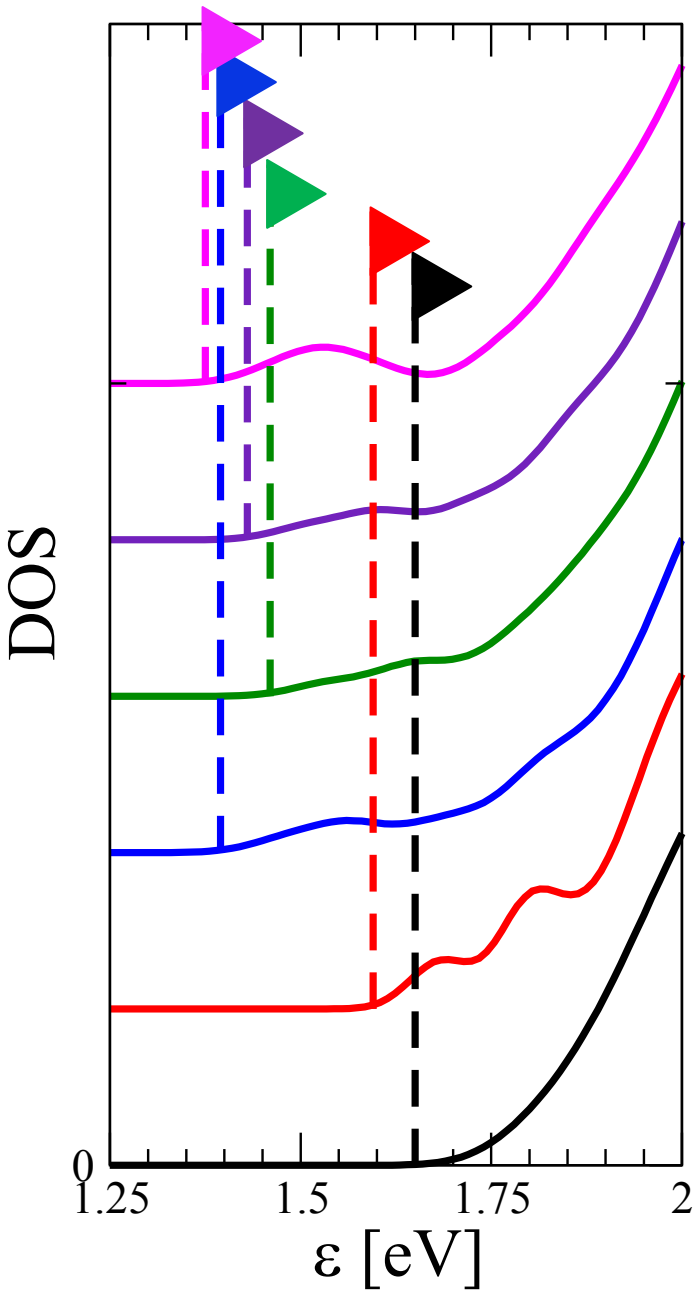

Figure S15. DOS of the five defect configurations in neutral charge state (i.e. when they captured an electron) compared with the one of the bulk system. The flag denoted the position of the conduction band minimum (CBM - black) and minimum energy of occupied defect states (flags of the same color of the line of the DOS of the defect). One notices that 4 out of 5 defect states present an occupied defect orbital at an energy > 0.25 (ten times the thermal energy at room temperature, 10 x k_BT) below the CBM. Thermal excitation of carriers captured in this orbital to be excited in the conduction band is much less likely than those laying in defect orbitals of defect type #1 (red curve), which is only 3 x k_BT below the CBM.

Figure S16 shows the DOS of the nominal defect $Bi_{Pb}^{\bullet}$ in the configuration 1 and 2 (we remark that this DOSes differ from the one of Figure S15 and Fig. **9** because here we compute them for defects in the +1 charged state, i.e. when the defect state is empty). The DOSes of the two configurations differ for the presence of the deep defect state in the configuration 2. Despite this, the dielectric functions of the two configurations are very similar, without any signature of the deep state (inset of Fig. **9a** and Figure S20). This confirms that the deep state is dark.

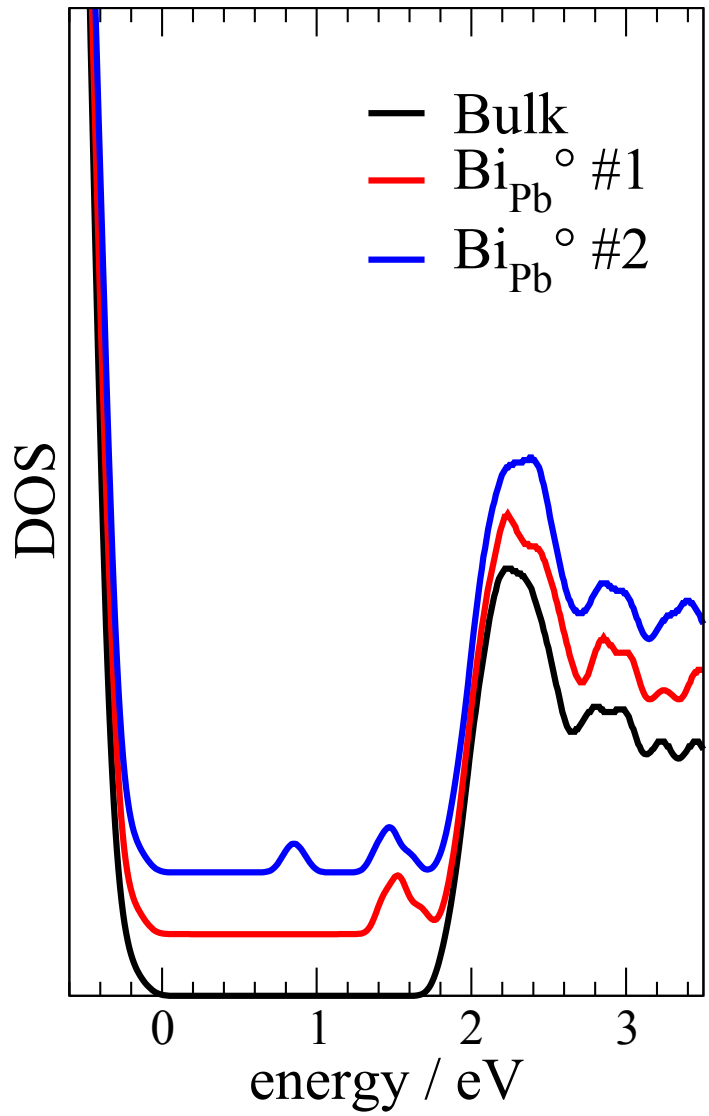

Figure S16. DOS of the positive charged defect of configurations 1 (red) and 2 (blue). One notices that the DOS of the two configurations are very similar in the energy range close to the VBM and CBM but they differ in the bandgap region, where the configuration 2 presents a peak corresponding to the deep state.

Bi_i defect: energetics, electronic structure and optical properties.

In the main text we gave arguments and bibliographic references explaining why interstitial bismuth defect is not likely to be formed and be responsible for the observed phenomenology. Nevertheless, we computed the thermodynamic transition energy level of this defect, which is E_{CBM} - ε (+/0)= 0.24 eV. Figure S17 shows the DOS of a system containing Bi_i, which gives a picture consistent with this value of the transition energy level: in the neutral charge state the system has a peak corresponding to the half-filled defect orbital at ~ 0.28 eV below the conduction band.

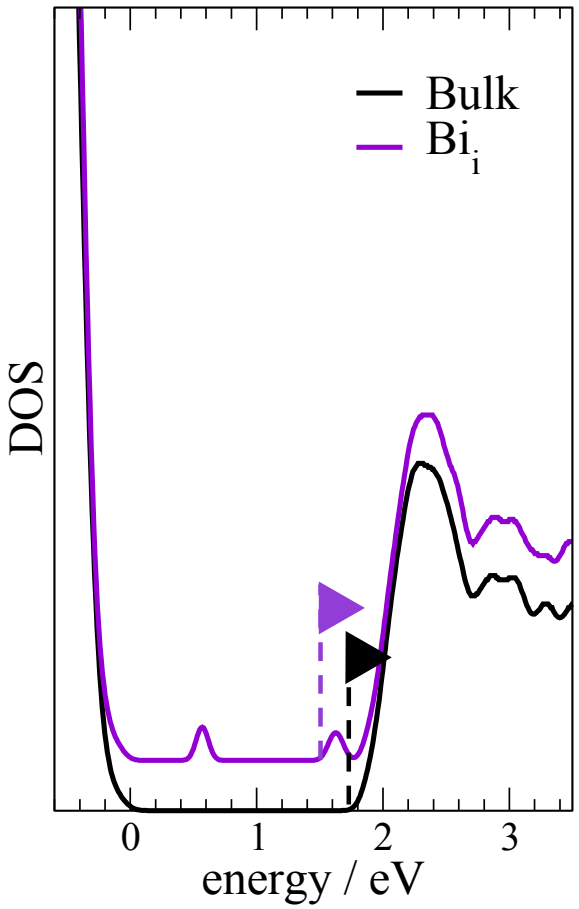

Figure S17. DOS of the neutral Bi_i defect. The DOS presents two gap states of which the higher in energy, at ~ 0.28 eV below the CBM, is half-filled.

At a variance with $Bi_{Pb}^{\bullet}$, $Bi_i^{\bullet}$ presents no empty states near the CBM, but it has filled states slightly above the VBM (Figure S20a). Thus, in principle $Bi_i^{\bullet}$ might show low energy tails associated to the transition from Bi-related filled state above the VBM into the conduction band. However, the calculated dielectric function of this system overlaps with the bulk case (Figure S20b), indicating that $Bi_i^{\bullet}$ cannot be the defect responsible for the spectroscopic signals measured in the experiments.

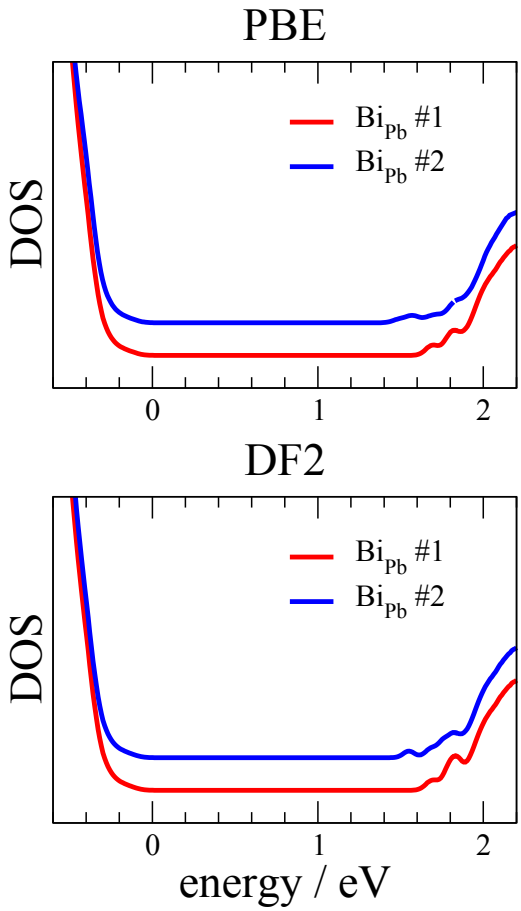

Figure S18. Effect of van der Waals interactions on the DOS of deep and shallow Bi_{Pb} defects: comparison between PBE and vdW-DF2 results.[5] One notices that the DOS with and without van der Waals interactions show minimal differences that do not alter the conclusion of our work. This extends recent literature results on the minor effect of van der Waals interactions on several properties of lead halide perovskites.[3,6]

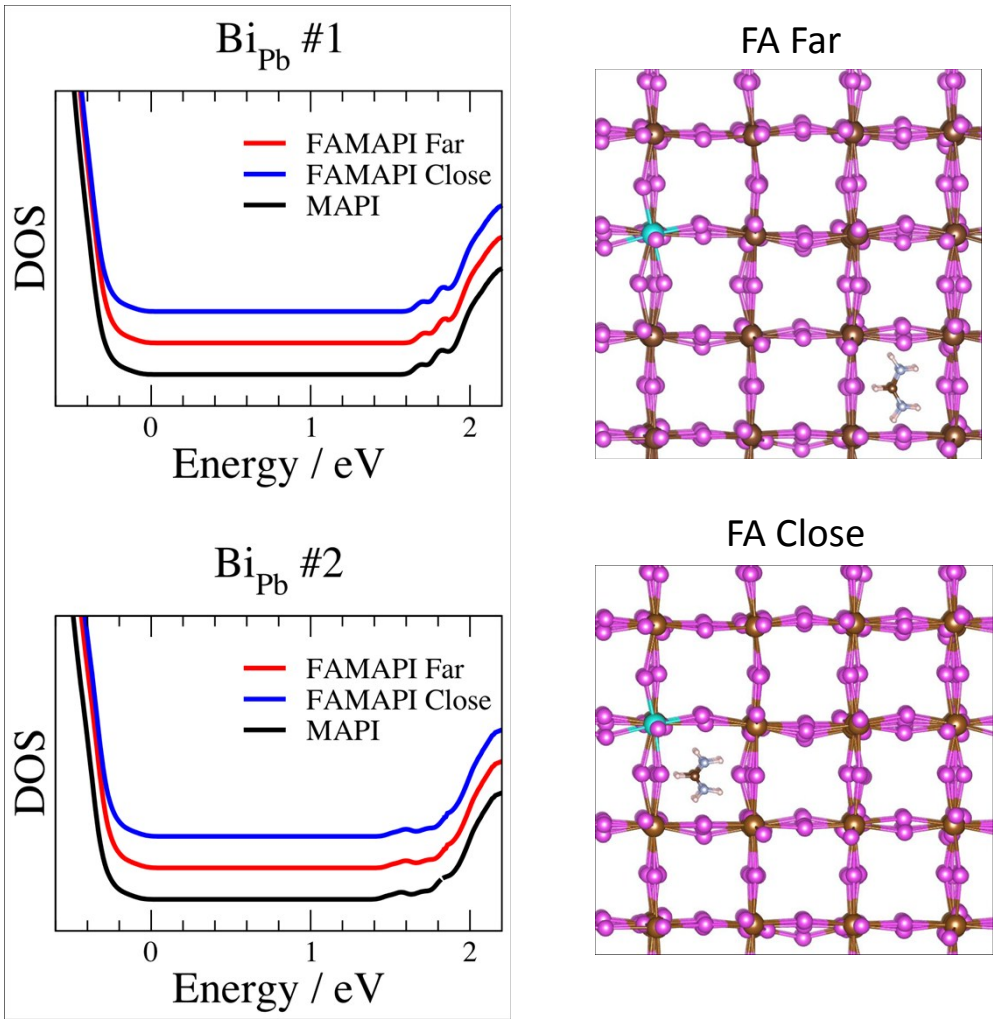

Figure S19. Effect of cation mixing on the DOS of shallow (top) and deep (bottom) Bi_{Pb} defects. We consider two cases, when FA^+ cation is i) close and ii) far from Bi_{Pb}. One notices that the DOS of pure MAPI and FAMAPI with the FA+ ion close and far from Bi_{Pb} are essentially indistinguishable, with a shifting of the DOS among the three cases within few 10s of meV, i.e. within the DFT accuracy. In particular, in FAMAPI one observes a very tiny reduction of the bandgap with a shift of the valence band toward slightly higher energies (the Pb-5d semi-core orbitals has been used as internal reference as described in Ref. [2]). This is consistent with the effect of the bulkier monovalent cation.

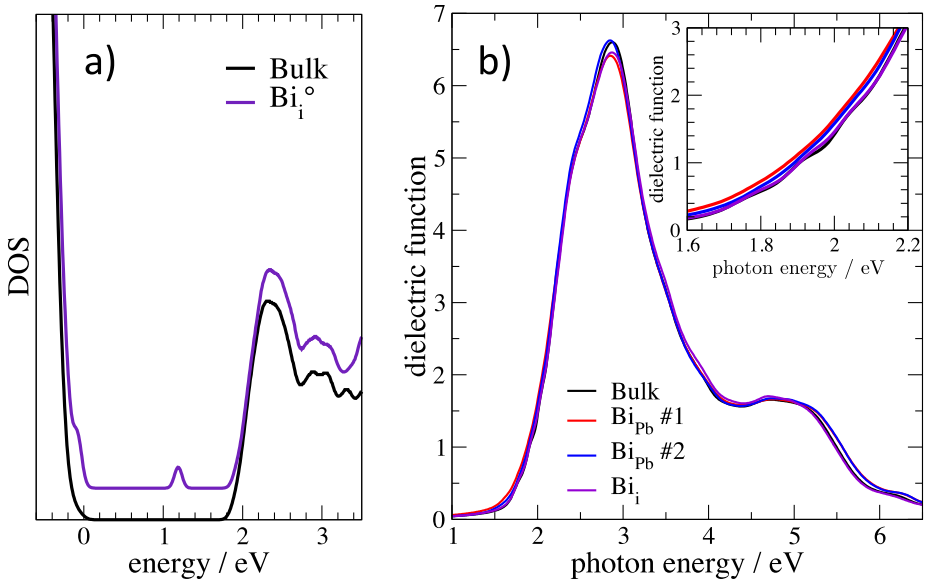

Figure S20. a) DOS of the +1 interstitial bismuth, $Bi_i^\bullet$ (violet) compared with the corresponding function of bulk $CH_3NH_3PbI_3$ (black). The DOS of $Bi_i^\bullet$ is characterized by filled orbitals near the edge of the valence bands and an empty state in the bandgap. b) Dielectric function of bulk $CH_3NH_3PbI_3$ (black), $Bi_{Pb}^\bullet$ in configuration 1 (red) and 2 (blue) and $Bi_i^\bullet$ (violet). The $Bi_i^\bullet$ perfectly overlaps with the bulk case. In particular, there is no low energy tails, as highlighted by the zoom shown in the inset.

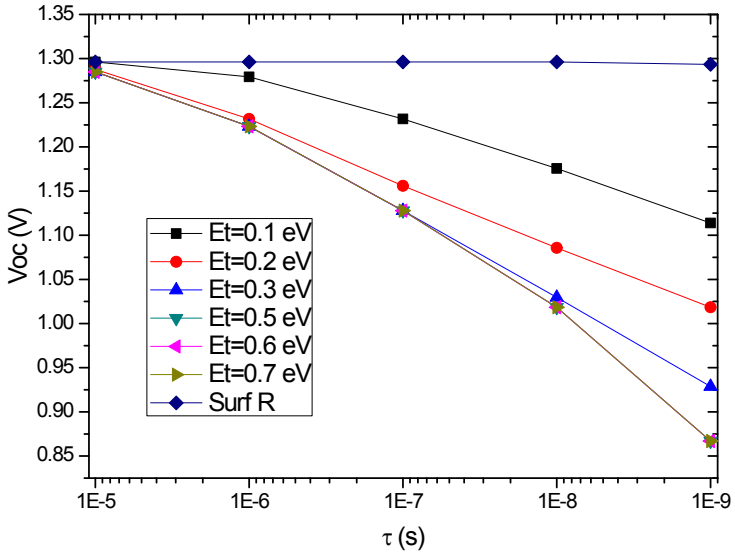

Figure S21. Simulated open-circuit voltage vs. charge carrier lifetime for different energies of a single trap level assuming SRH recombination in the absorber layers. Surf R means SRH recombination in regions (5 nm) close to the contacts. Details on the input parameters are found in Table S3.

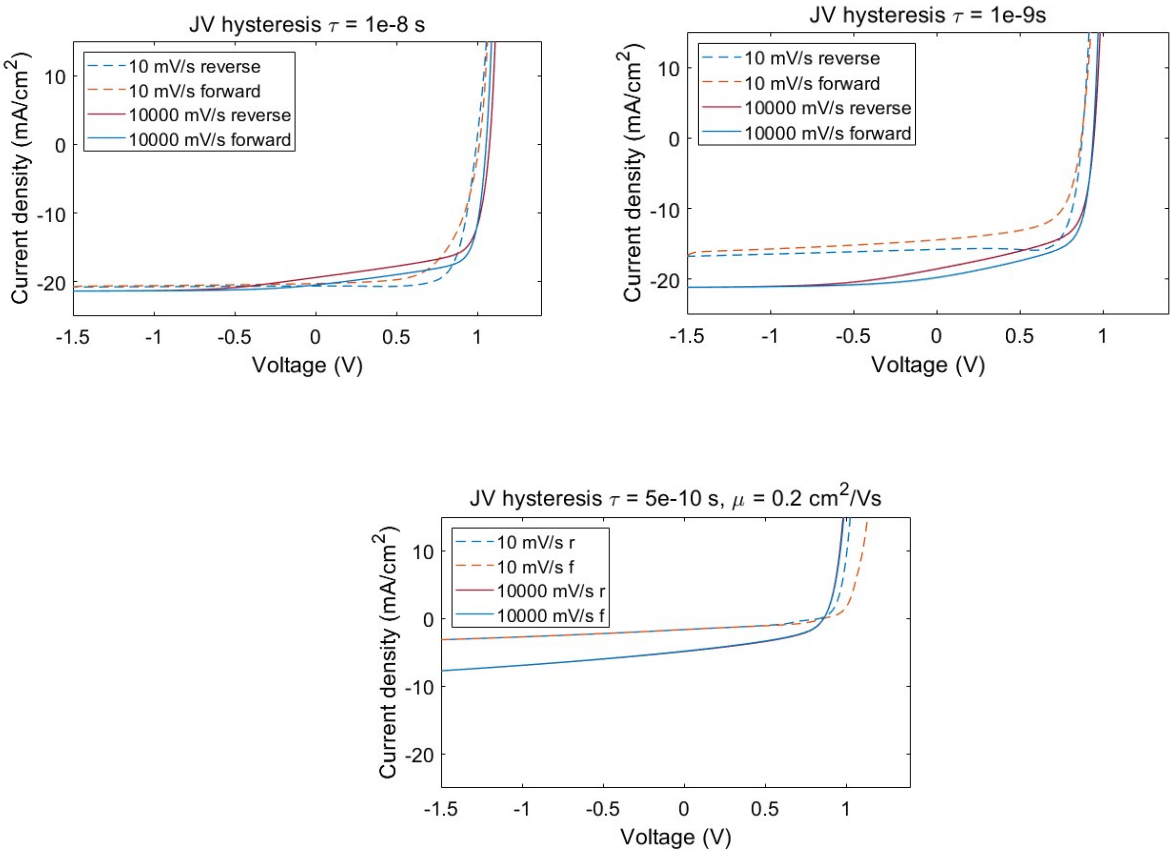

Figure S22. Scan-rate dependence of the simulated *J-V* hysteresis (initial equilibration at positive voltage). Enhanced recombination reduces the photocurrent for lower scan rates as seen in experiment in Fig. 3 of the main manuscript. An additional decrease of the mobility (bottom) leads to a reduction of the fill factor and traces that are similar to the experimental data of devices containing 1% Bi. Details on the input parameters are found in Table S3.

Table S1. Lattice parameters of Bi-doped mixed-cation perovskite thin-films.

Batch 1				
Bi%	*a* (Å)	esd.	V (Å^3)	esd.
0	6.26505	0.0015	245.9088	0.17606
0.1	6.26278	0.00113	245.6418	0.13298
0.25	6.26016	0.00134	245.3336	0.15761
0.5	6.25372	0.00373	244.5768	0.43719
1	6.24954	0.00287	244.0864	0.33657
2	6.25329	0.00289	244.5259	0.33887
Batch 2				
Bi%	*a* (Å)	esd.	V (Å^3)	esd.
0	6.27355	0.00573	246.9110	0.67703
0.1	6.26773	0.00479	246.2247	0.56450
0.25	6.26305	0.00353	245.6731	0.41546
0.5	6.26392	0.00701	245.7754	0.82498
1	6.25429	0.00124	244.6435	0.14577
2	6.25566	0.00258	244.8050	0.30330

Table S2. Lattice parameters of Bi-doped mixed-cation perovskite thin-films measured with grazing incidence X-ray diffraction under two angles of incidence: 0.25° and 1°

Surface	[Bi]	Lattice parameters, *a*/Å	Esd. *a*/Å	Cell volume, *V*/Å^3	Esd. *V*/Å^3
	0.25%	6.26247	0.00072	245.60508	0.08492
	2%	6.26388	0.00086	245.77082	0.101
	0%	6.26970	0.00057	246.45698	0.06725
Bulk					
	0.25%	6.26499	0.00021	245.90123	0.02469
	2%	6.26618	0.00029	246.04174	0.0345
	0%	6.27375	0.00021	246.93388	0.02509

Table S3. Parameters used for the drift-diffusion simulation.

Parameter	Description	Value
ε_r	Relative permittivity	[4,23,12][1]
L	Device thickness	[150, 500, 200] [1] nm
EA	Electron affinity	[1.9, 3.8, 4.1] [1] eV
IP	Ionization energy	[5.1, 5.4, 7.4] [1] eV
E0	Equilibrium Fermi Level	[-5.0, -4.6, -4.2] [1] eV
μ	Electron and hole mobilities	[0.02, 20, 0.09][1] $cm^2V^{-1}s^{-1}$
k	Direct recombination rate	[3.17×10^{-11}, 3.6×10^{-12}, 1.5×10^{-10}][1] cm^2s^{-1}
W_A	Work-function of anode	5.0 eV
W_C	Work-function of cathode	4.2 eV
N_0	Effective density of states	10^{19} cm^{-3}
N_i	Mobile ionic defect density	10^{17} cm^{-3}
μ_i	Ionic defect mobility	10^{-10} $cm^2V^{-1}s^{-1}$
G	Generation rate in perovskite for 1 Sun illumination	2.64×10^{21} $cm^{-3}s^{-1}$
T	Temperature	300 K

[1] in the sequence of HTL/perovskite/ETL

REFERENCES

(1) Yin, W.-J.; Shi, T.; Yan, Y. Unusual Defect Physics in CH3NH3PbI3 Perovskite Solar Cell Absorber. *Appl. Phys. Lett.* **2014**, *104* (6), 63903.

(2) Meloni, S.; Palermo, G.; Ashari-Astani, N.; Grätzel, M.; Rothlisberger, U. Valence and Conduction Band Tuning in Halide Perovskites for Solar Cell Applications. *J. Mater. Chem. A* **2016**, *4* (41), 15997–16002.

(3) Ashari-Astani, N.; Meloni, S.; Salavati, A. H.; Palermo, G.; Grätzel, M.; Rothlisberger, U. Computational Characterization of the Dependence of Halide Perovskite Effective Masses on Chemical Composition and Structure. *J. Phys. Chem. C* **2017**, *121* (43), 23886–23895.

(4) Harrison, W. A. *Solid State Theory*; 2011.

(5) Lee, K.; Murray, É. D.; Kong, L.; Lundqvist, B. I.; Langreth, D. C. Higher-Accuracy van Der Waals Density Functional. *Phys. Rev. B* **2010**, *82* (8), 081101.

(6) Pérez-Osorio, M. A.; Champagne, A.; Zacharias, M.; Rignanese, G.-M.; Giustino, F. Van Der Waals Interactions and Anharmonicity in the Lattice Vibrations, Dielectric Constants, Effective Charges, and Infrared Spectra of the Organic–Inorganic Halide Perovskite CH3NH3PbI3. *J. Phys. Chem. C* **2017**, *121* (34), 18459–18471.